The Effect of Resonance Absorption in OMEGA Direct-Drive Designs and Experiments

Introduction

Ignition of thermonuclear fuel (DT mixture) requires a fuel areal density $\gtrsim 0.3$ g/cm^2 and a hot-spot temperature $\gtrsim 10$ keV (Refs. 1 and 2). Such conditions are predicted to be achieved in direct-drive inertial confinement fusion (ICF) designs, in which a cryogenic spherical DT-ice-shell target is imploded using direct illumination by intense laser beams.[3–7] High energy gain in direct-drive ICF designs is achieved by optimizing the laser pulse shape and target dimensions.[1,8,9]

Physical understanding of laser–plasma coupling is required for accurate numerical modeling of high-gain, direct-drive ICF designs. These designs are based on precise timing of laser-driven shocks, which determine the target adiabat (defined as a ratio of the fuel pressure to the Fermi-degenerate pressure).[10,11] The shock strength depends crucially on mechanisms of laser light absorption. A theoretical and experimental investigation of laser absorption, focusing on the effect of resonance absorption for typical conditions in the direct-drive experiments on the OMEGA Laser System,[12] is the subject of this article.

Resonance absorption of electromagnetic waves in an unmagnetized, inhomogeneous plasma has been of considerable interest for a long time.[13–25] In this process, a p-polarized electromagnetic wave, i.e., a wave that has a nonzero electric field component along the electron-density gradient ∇n_0, propagates from low to high densities and approaches the critical surface with an electron density $n_0 = n_{cr}$, where the laser frequency ω matches the local electron plasma frequency $\omega_{pe} = 4\pi n_0 e^2 / m_e$. Here, e and m_e are the electron charge and mass, respectively. During this propagation, the wave is partially reflected from the turning point, defined by the condition $\omega_{pe} = \omega \cdot \cos\theta$, where θ is the angle between the vacuum wave vector **k** and the density gradient, and the small part of the wave energy tunnels to the critical density and excites the resonance plasma oscillations. These oscillations can be damped by various mechanisms, including electron–ion collisional damping and excitation of Langmuir waves. A one-dimensional model of resonance absorption in linear density profiles has been the subject of numerous analytical and numerical investigations. Forslund *et al.*[19] solved numerically the wave equation for the electric field **E** and found the absorption fraction of electromagnetic waves as a function of $q \equiv (kL)^{2/3} / \sin^2\theta$, where L is the density scale length. This result was confirmed later by the simulations of Pert[21] and Means *et al.*,[22] who employed different methods. All of these numerical results agree well with analytic results obtained by Omel'chenko and Stepanov,[16] Speziale and Catto,[20] and Tang[17] for limited ranges of q. An analytic expression for the absorption fraction in the whole range of q was obtained by Hinkel–Lipsker *et al.*[23] in the limit of small thermal and collisional effects. Later, the same authors[24] found analytic solutions of the problem in the case of parabolic density profiles. In our current numerical study, we do not restrict ourselves by linear or parabolic density profiles using density profiles obtained in hydrodynamic simulations. A recent study by Xu *et al.*[25] concentrated on modifications in resonance absorption caused by the relativistic effect and pondermotive force.

Direct-drive experiments conducted on OMEGA are routinely simulated using the 1-D hydrodynamic code *LILAC*.[26] The standard laser-absorption algorithm in *LILAC* is the ray-trace algorithm with ion–electron collisional absorption (inverse bremsstrahlung). An optional semi-analytic model of resonance absorption[27] can be used in conjunction with the ray-trace algorithm. An advantage of this semi-analytic model is its simplicity, whereas a disadvantage is its insufficient accuracy: it typically overestimates the resonance absorption by a factor of ~2 (Ref. 27). In this study, to more accurately investigate resonance absorption, the ray-trace algorithm of laser absorption in *LILAC* is replaced by a new algorithm based on the numerical solution of a wave equation in planar geometry.

This article addresses the following issues: (1) The wave equation describing the steady-state structure of electromagnetic and Langmuir wave components in inhomogeneous plasma is presented, and the numerical method in the planar geometry is described. (2) The results of numerical simulations of the resonance absorption in OMEGA plasmas are presented in the case of both planar and spherical geometries. (3) The

results of planar reflection light experiments on OMEGA are presented and compared with simulations, and a design of planar shock-timing experiments is considered. (4) The main results are discussed and summarized in the final section.

Resonance Absorption in the Fluid Approximation

We consider an electromagnetic wave of frequency ω propagated in vacuum, which obliquely irradiates a slab of warm, unmagnetized plasma. Properties of the slab are assumed to vary with a characteristic scale length $>> c/\omega$. Neglecting ion and low-frequency electron motions, one can describe a high-frequency electron motion caused by the electromagnetic wave using the linearized momentum equation

$$\frac{\partial \mathbf{u}_e}{\partial t} = -\frac{1}{m_e n_0}\nabla P_e - \frac{e}{m_e}\mathbf{E} - \nu \mathbf{u}_e, \tag{1}$$

where $\mathbf{u}_e$ is the velocity and P_e is the pressure of electrons, $\mathbf{E}$ is the electric field, and ν is the damping rate. Assuming a polytropic equation of state (e.g., Ref. 28), $P_e \propto n^3$, where n is the electron density, and a time variation of all perturbed quantities $\propto e^{-i\omega t}$, and combining Eq. (1) with the Poisson equation $\nabla \cdot \mathbf{E} = -4\pi e n$, we derive the expression for the current density

$$\mathbf{j} = -en_0\mathbf{u}_e = i\frac{\omega_{\mathrm{pe}}^2 \mathbf{E}}{4\pi(\omega + i\nu_{\mathrm{em}})} - i\frac{3v_e^2 \nabla(\nabla \cdot \mathbf{E})}{4\pi(\omega + i\nu_w)}, \tag{2}$$

where $v_e^2 = T_e/m_e$ is the electron thermal velocity square and T_e is the electron temperature. In Eq. (2), two different damping rates ν_{em} and ν_w have been introduced instead of the single damping rate ν in Eq. (1) (see Ref. 19). The rate ν_{em} corresponds to the electromagnetic and ν_w to the Langmuir wave components represented by the first and second terms on the right-hand side of Eq. (2), respectively. The electric field $\mathbf{E}$ obeys Maxwell's equations, which can be reduced to the steady-state wave equation

$$\nabla^2 \mathbf{E} - \nabla(\nabla \cdot \mathbf{E}) + \frac{\omega^2}{c^2}\left(\mathbf{E} + i\frac{4\pi}{\omega}\mathbf{j}\right) = 0, \tag{3}$$

where $\mathbf{j}$ is defined by Eq. (2). Solving Eq. (3) with respect to $\mathbf{E}$, one can calculate the laser-absorption rate $Q = \mathbf{j} \cdot \mathbf{E}$. With the help of Eq. (2), Q can be expressed in the following form:

$$Q = Q_{\mathrm{em}} + Q_w = \nu_{\mathrm{em}}\frac{\omega_{\mathrm{pe}}^2}{\omega^2 + \nu_{\mathrm{em}}^2}\frac{\mathbf{E}^2}{8\pi} + \nu_w\frac{3v_e^2}{\omega^2 + \nu_w^2}\frac{(\nabla \cdot \mathbf{E})^2}{8\pi}. \tag{4}$$

This form allows one to distinguish the different contributions to laser absorption: the electromagnetic Q_{em} and Langmuir wave Q_w components. The damping rate ν_{em} is determined by the collisional damping, $\nu_{\mathrm{em}} = \nu_{\mathrm{ei}}$ (Ref. 2). The damping rate ν_w, in addition to collisional damping, must include damping due to kinetic effects, which describe dissipation of Langmuir waves at $k\lambda_{\mathrm{D}} \gtrsim 1$, where k is the wave number and λ_{D} is the Debye length. This gives $\nu_w = \nu_{\mathrm{ei}} + \nu_{\mathrm{L}}$, where

$$\nu_{\mathrm{L}} = \left(\frac{27\pi}{8}\right)^{1/2}\frac{\omega_{\mathrm{pe}}^2\omega^2}{\left(\omega^2 - \omega_{\mathrm{pe}}^2\right)^{3/2}}e^{-\frac{3}{2}\frac{\omega^2}{\omega^2 - \omega_{\mathrm{pe}}^2}} \tag{5}$$

is the Landau damping rate.[29]

We consider planar geometry and introduce the cartesian coordinates (x, y, z) with the z axis perpendicular to the plane of the plasma slab. The slab is uniform in the x and y directions and nonuniform in the z direction. The vacuum wave vector $\mathbf{k}$ of the incident plane electromagnetic wave is located in the y–z plane and inclined at an angle θ with the z axis. In these coordinates, the s-polarized electromagnetic wave is described by a solution E_x of the x component of Eq. (3). This solution is completely independent of a solution for the p-polarized wave described by E_y and E_z, which obey the coupled y and z components of Eq. (3). Assuming an independence of the field of the x coordinate and periodic dependence on the y coordinate, $\propto e^{ik_y y}$, where $k_y = (\omega/c)\sin\theta$, the corresponding components of Eq. (3) can be reduced to second-order ordinary differential equations in the following form: for the s-polarized wave,

$$\frac{\mathrm{d}^2 E_x}{\mathrm{d}z^2} + \frac{\omega^2}{c^2}\left(\epsilon - \sin^2\theta\right)E_x = 0, \tag{6}$$

and for the p-polarized wave,

$$\frac{\mathrm{d}^2 E_y}{\mathrm{d}z^2} - ik_y(1-\eta)\frac{\mathrm{d}E_z}{\mathrm{d}z} + \frac{\omega^2}{c^2}\left(\epsilon - \eta\sin^2\theta\right)E_y = 0, \tag{7}$$

$$\eta \frac{\mathrm{d}^2 E_z}{\mathrm{d}z^2} - ik_y(1-\eta)\frac{\mathrm{d}E_y}{\mathrm{d}z} + \frac{\omega^2}{c^2}\left(\epsilon - \sin^2\theta\right)E_z = 0\,, \qquad (8)$$

where we use the notations

$$\epsilon = 1 - \frac{\omega_{\mathrm{pe}}^2}{\omega\left(\omega + i\nu_{\mathrm{em}}\right)} \text{ and } \eta = \frac{3v_e^2}{\omega\left(\omega + i\nu_w\right)}\frac{\omega^2}{c^2}.$$

These differential equations are solved using the standard finite-difference numerical technique, which requires the solution of linear matrix equations. The matrix equations have a band diagonal form and can be efficiently solved by the LU decomposition method.[30] We assume vacuum boundary conditions for the incident and reflected electromagnetic waves at the outer edge of the plasma corona. For example, these conditions for the *s*-polarized wave are derived by using a vacuum solution in the form $E_x = Ae^{ik_z z} + Be^{-ik_z z}$, where $k_z = (\omega/c)\cos\theta$, and the complex coefficients A and B to be determined matching this solution and its first derivative with the corresponding numerical solution at the outer edge. Similarly, other solutions of the electric field, E_y and E_z, are considered in the case of the *p*-polarized wave. Knowing the field components, one can calculate the laser-absorption rate using Eq. (4) as the energy source in a 1-D hydrodynamic code.

Resonance Absorption in Typical OMEGA Plasmas

The 60-beam, 30-kJ OMEGA Laser System[12] is used to study the physics of implosions by conducting spherical and planar experiments with millimeter-scale targets. OMEGA operates at a laser wavelength of $\lambda = 351$ nm and peak intensities varying from 10^{14} to 10^{15} W/cm^2 with a typical pulse rise time ~100 ps and a pulse duration ~1 to 3 ns. The pulse can be shaped to optimize target performance.[10,11]

In this section we investigate numerically the effects of resonance absorption for plasma conditions relevant to direct-drive OMEGA experiments. Currently, plastic (CH) material is used as an ablator in most applications;[7] therefore, we concentrate our analysis on CH plasma. All numerical results reported hereafter are obtained by employing the flux-limited Spitzer–Härm thermal-conduction model.[26,31] If not explicitly mentioned, simulations assume a flux-limiter value $f_{\mathrm{lim}} = 0.06$, and all of our numerical results include the Langdon effect.[32] Note that other more-sophisticated thermal-conduction models can be used, including the models based on the solution of the Fokker–Planck equation[33] and different nonlocal electron transport treatments[34,35] We found, however, that the effect of resonance absorption is not very sensitive to the particular choice of the thermal-conduction model.

The method of laser-absorption simulation described in the previous section was developed in planar geometry, where the incident light can be properly separated on the *s*- and *p*-polarized components. In spherical geometry, such a separation is not possible and the exact solution of the problem is more complicated. Instead of exactly solving the problem in spherical geometry, an approximate approach can be used to estimate laser absorption with the resonance effect. In the following two subsections we consider first the case of planar geometry, in which the effect of resonance absorption is calculated using the exact method; we then consider the case of spherical geometry, applying the planar-geometry approximation.

1. Planar Geometry

Figure 111.45 shows an example of a simulated electric field in a plasma developed during irradiation of a thick CH foil by a single *p*-polarized OMEGA laser beam with an angle of incidence $\theta = 23.2°$. This angle is typically used in planar OMEGA experiments and close to the angle at which resonance absorption is most effective (see the definition of this angle below). The drive laser pulse [Fig. 111.45(a)] is taken from the actual experiment and has a square shape with about 1-ns duration, an average intensity $I \approx 5 \times 10^{14}$ W/cm^2, and an initial rise time ≈100 ps. The intensity modulation seen in Fig. 111.45(a) is due to the effect of smoothing by spectral dispersion.[36] The solutions shown in Fig. 111.45(b) correspond to the time when the pulse intensity reaches the average value at $t = t_0$. The distribution of electron density n_0 [shown by the thick line in Fig. 111.45(b)] is obtained using a *LILAC* simulation. The incident laser light propagates from right to left. The electron temperature $T_e \approx 1$ keV at the critical surface, which is defined by the condition

$$n_0 = n_{\mathrm{cr}} \equiv \frac{m_e\omega^2}{4\pi e^2} \approx 9 \times 10^{21}\left(\frac{351\,\mathrm{nm}}{\lambda}\right)^2 \mathrm{cm}^{-3}. \qquad (9)$$

The value of T_e varies insignificantly on the spatial interval displayed in Fig. 111.45(b). The solution shown by the thin solid line is obtained including all terms in Eq. (1). This solution shows some increase in the electric field near the critical surface and, at the same time, shows a resonant excitation of Langmuir waves. These waves can be clearly seen in Fig. 111.45(b) as the short-wavelength structures at $z \approx 64\ \mu$m, whereas the long-wavelength structures at $z > 64\ \mu$m correspond to electromagnetic waves. The Langmuir

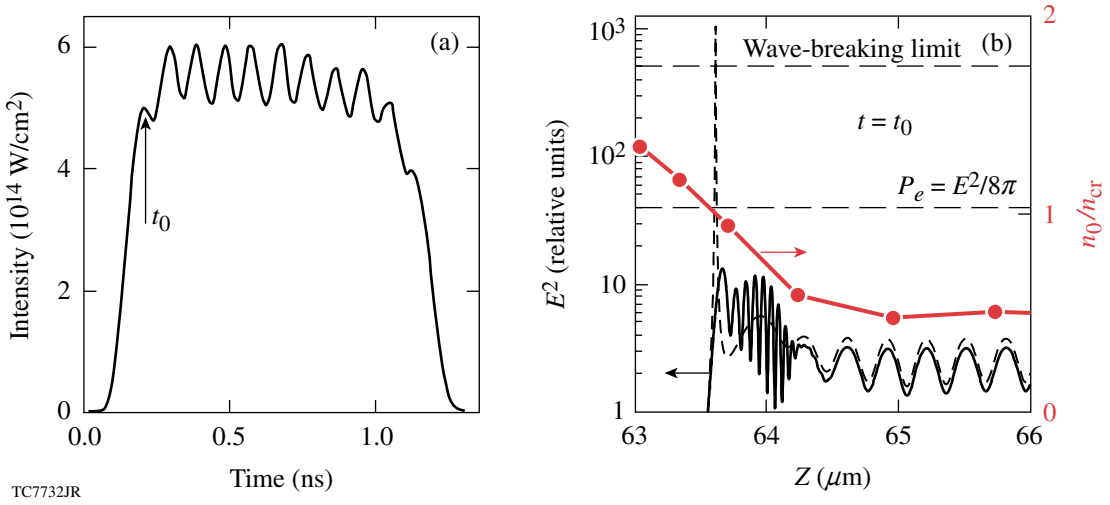

Figure 111.45
Example distribution of the electric field in a CH plasma near the critical surface, $n_0 = n_{cr}$. (a) The drive laser pulse irradiated a thick planar CH target at θ = 23.2°; the vertical arrow shows time t_0 and laser intensity for solutions presented in plot (b). (b) Distributions of the electron density n_0 and squared amplitude of the electric field $E^2 = E_y^2 + E_z^2$. Laser light with p-polarization propagates from right to left. The distribution of n_0 (thick solid line) is obtained using a 1-D *LILAC* simulation. The electron temperature near the critical surface is ≈1 keV. The thin solid and short-dashed lines show the distribution of E^2 obtained with and without the pressure term in Eq. (1), respectively. The two horizontal dashed lines represent the estimates of the wave-breaking and thermal pressure limits for E^2.

waves propagate from the critical surface to the right, toward the lower electron density, and decay due to Landau damping at $n_0 \lesssim 0.6\, n_{cr}$ (the "wave-decay" region). Landau damping results in a conversion of the energy stored in Langmuir waves into hot electrons with $T_h \approx 5$ keV, where the latter temperature is estimated using the phase velocity of Langmuir waves in the wave-decay region. Heating of the plasma [see Eq. (4)] occurs due to both collisional and Landau damping and is localized mainly between the critical surface and the wave-decay region. A typical electron temperature in the hot corona is about 1 to 2 keV, which is 2 to 5 times lower than our estimate of T_h. This could result in a deviation of the electron distribution function from Maxwellian and nonlocal effects in the energy deposition. In our simulations, however, we neglect such nonlocal effects and assume only the local energy deposition into thermal electrons. For comparison, the solution without excitation of Langmuir waves is shown by the short-dashed line in Fig. 111.45(b). This solution, obtained using Eq. (1) without the pressure term (the cold plasma limit), has a distinctive resonance peak in the electric field at the critical surface. Note that the resonant field in the latter case exceeds the limits for the field corresponding to the electron pressure P_e and wave-breaking threshold[37] [represented by the lower and upper horizontal dashed lines in Fig. 111.45(b), respectively].

Two important conclusions regarding plasma conditions in direct-drive OMEGA experiments result from the considered example: First, the resonant electric field in a typical OMEGA plasma is significantly below the wave-breaking limit. Second, the electromagnetic pressure corresponding to this field is typically below the electron pressure, which means that the pondermotive force is weak and can be neglected. These conclusions justify the omission of the nonlinear convection term $(\mathbf{u}_e\nabla)\mathbf{u}_e$ in Eq. (1).

Next, we study the time evolution of the resonance absorption and its dependence on laser intensity and incident angle. The resonance absorption in a simulation can be quantified by comparing the absorption rates for s- and p-polarized laser beams (Q^s and Q^p, respectively) since Q^p includes the effect of resonance absorption and Q^s does not. Figure 111.46 compares these absorption rates and also presents Q_w^p, which is the contribution to the absorption rate due to the resonant excitation of Langmuir waves [see Eq. (4)], calculated for the case of thick (>200 μm) CH foils irradiated by a 1-ns square pulse at θ = 23.2°. Three different average beam intensities have been considered: 10^{14}, 5×10^{14}, and 10^{15} W/cm^2. Figure 111.46(a) shows the laser pulse shape and absorption rates Q^s for these three cases. Figure 111.46(b) shows the relative difference $\left(Q^p - Q^s\right)/Q^s$ (solid lines), which characterizes the contribu-

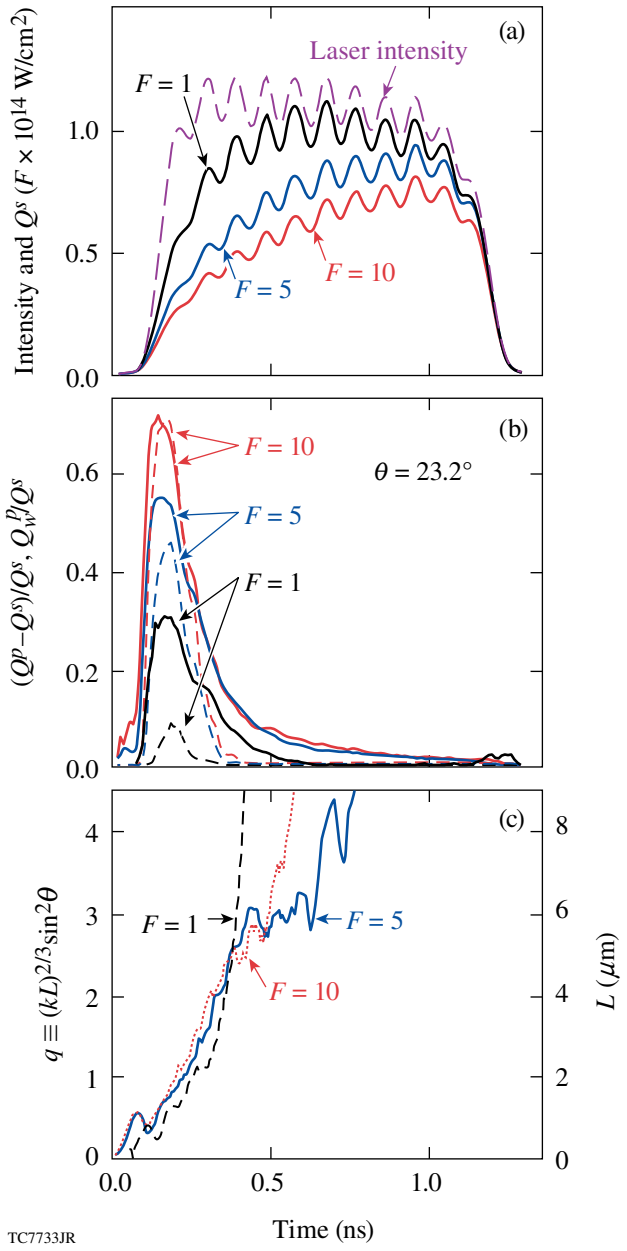

Figure 111.46
Simulated evolution of the laser-absorption rate for single, *s*- and *p*-polarized, 1-ns OMEGA laser beams irradiating a thick planar CH target at $\theta = 23.2°$. Three different average laser intensities are considered: 10^{14}, 5×10^{14}, and 10^{15} W/cm^2, which are indicated by the corresponding values of the scaling factor $F = 1$, 5, and 10, respectively. (a) Drive-laser pulse (long-dashed line) and absorption rates Q^s (solid lines) for the *s*-polarized beams. These rates do not include the effect of resonance absorption. (b) The relative differences between the absorption rates for *p*- and *s*-polarized beams $\left(Q^p - Q^s\right)/Q^s$ (solid lines), which demonstrate the effect of resonance absorption in the *p*-polarized beams, and the relative absorption rates Q_w^p/Q^s due to the resonant excitation of Langmuir waves (dashed lines). (c) Evolution of $q \equiv (kL)^{2/3}\sin^2\theta$ and the density scale length L at the critical surface. The resonance absorption is important as soon as $0.1 < q < 2$ (Ref. 19).

tion of resonance absorption to the total laser absorption, and the ratio Q_w^p/Q^s (dashed lines). The results show that the effect of resonance absorption is important only in the initial 200- to 300-ps period of the laser pulse. This time dependence can be explained by the inverse dependence of resonance absorption on the density scale length L near the critical surface. Figure 111.46(c) shows the evolution of L and the dimensionless quantity $q \equiv (kL)^{2/3}\sin^2\theta$, where k is the vacuum wave number of laser light. The resonance absorption can be efficient if $0.1 \lesssim q \lesssim 2$ (Ref. 19). The density scale length is relatively short, $L \approx 1$ to 2 μm (so $q < 2$), during the rise of laser power. At a later time, at maximum laser power, the length becomes long enough, $L > 5$ μm ($q > 2$), to quench the resonance absorption. Another effect seen in Fig. 111.46(b) is that the resonance absorption, including absorption via Langmuir waves, is more significant for higher laser intensities. In particular, the resonance mechanism dominates over inverse bremsstrahlung at the beginning of the laser pulse for pulses with peak intensity $\gtrsim 5 \times 10^{14}$ W/cm^2. The dependence of resonance absorption on the intensity can be attributed to increased temperature near the critical surface in the case of higher laser intensities.[19]

The angular dependence of resonance absorption is demonstrated in Fig. 111.47, where the results of simulations are shown for a 100-ps laser pulse. For such a short pulse, the contribution of resonance absorption to the total absorption is more prominent and can be more easily measured experimentally (see Fig. 111.46). A laser pulse with a peak intensity of 5×10^{14} W/cm^2 is shown by the long-dashed line in Fig. 111.47(a). In the same figure, example absorption rates in the case of *p*- and *s*-polarized laser beams (thick and thin lines, respectively) and resonant excitation of Langmuir waves in the *p*-polarized beam (short-dashed line) are shown for $\theta = 17°$. Figure 111.47(b) plots the angular dependence of absorption fractions in the case of *p*- and *s*-polarized beams and resonant excitation of Langmuir waves, using the same notations as in Fig. 111.47(a). Here, the absorption fraction is defined as the ratio of the corresponding time-integrated absorption rate per unit surface to the time-integrated laser intensity on target. The difference between the absorption fractions for *p*- and *s*-polarized beams illustrates the relative effect of resonance absorption. This effect peaks at $\theta \approx 17°$ and corresponds to about a 30% increase in total absorption in comparison with the case of *s*-polarized beams. The energy absorbed due to the resonant excitation of Langmuir waves also peaks at $\theta \approx 17°$, where the contribution of this energy to the total absorption energy is about 50%.

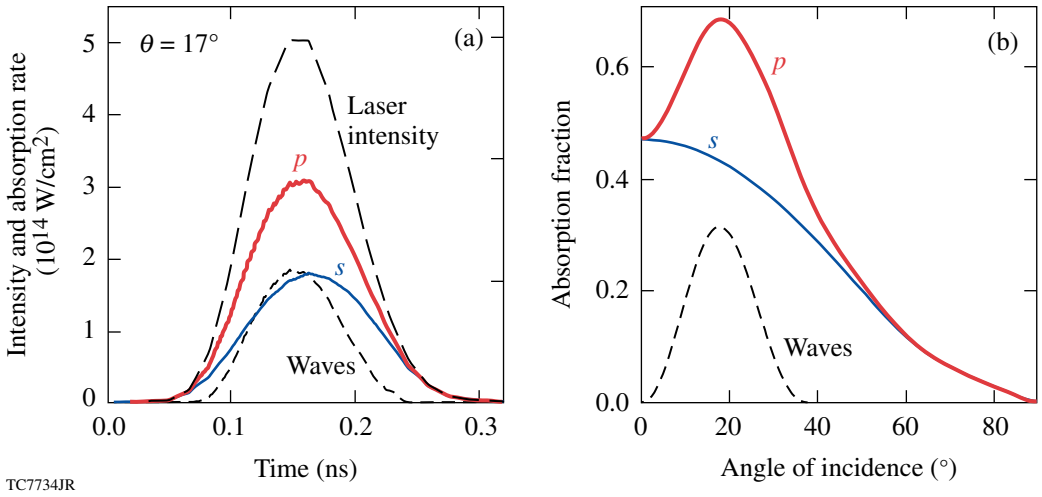

Figure 111.47
Simulated absorption rate and angular dependence of absorption fraction for single, *s*- or *p*-polarized, 100-ps OMEGA laser beams irradiating a thick planar CH target. (a) Drive-laser pulse with a peak intensity of 5×10^{14} W/cm^2 (long-dashed line); the absorption rate for the *p*- and *s*-polarized beams (thick and thin solid lines, respectively), and the absorption rate due to the resonant excitation of Langmuir waves (short-dashed line). All of these rates are calculated assuming $\theta = 17°$. (b) Time-integrated absorption fractions as functions of θ in the same cases considered in (a). The effect of resonance absorption is represented by the difference in absorption rates and absorption fractions for the *p*- and *s*-polarized beams. This effect produces the maximum absorption fraction at $\theta \approx 17°$.

2. Spherical Geometry

In this section, we use an approximate approach to estimate the laser absorption, including the resonance effect, in spherical implosions. We apply the planar method to a small surface element of a spherical target. Such an element is irradiated by the laser light distributed over a range of incident angles θ from 0° to 90°. The total absorption rate for a target can be estimated by integrating the absorption rates for a given surface element over θ from all angles in the hemisphere that cover the surface element and integrating the result over the entire target surface. This approach can be justified if the thickness of the absorption region is much smaller than the target radius. Such a condition typically occurs during the first few hundred picoseconds in direct-drive OMEGA implosions.

The intensity profile $I(r)$ across an individual OMEGA laser beam can be approximated by the super-Gaussian[38] $I(r) = I_0 e^{-(r/r_0)^n}$, where I_0 is the center beam intensity, r is the distance from the beam's central axis, r_0 is the beam radius, and n is the super-Gaussian index. Assuming spherically symmetric illumination of a target of radius R, it is straightforward to obtain the angular-dependent laser intensity at each point of the target surface, $I(\theta) = I_0 e^{-(\sin\theta \cdot R/r_0)^n}$. Then, the intensity on target is

$$\overline{I} = 2\pi \int_0^{\pi/2} I(\theta) \cos\theta \sin\theta d\theta. \quad (10)$$

The angular distribution $I(\theta)$ is used in the modified planar method in *LILAC* to numerically estimate the laser-absorption rate Q in spherical implosions. To account for a mixed polarization of laser light from many randomly polarized OMEGA laser beams (up to 13 beams can irradiate a given small surface element), the method assumes an equal mixture of *s*- and *p*-polarized lights. The corresponding absorption rate is denoted as $Q^{s,p}$. The absorption rate calculated using only the *s*-polarized light, Q^s, does not include the effect of resonance absorption and is used for comparison. Note that, with respect to the assumed laser-absorption mechanisms, Q^s is similar to the absorption rate calculated using the spherical ray-trace method.[26]

Figure 111.48 shows an example of simulated laser-absorption rates in the spherical implosion of a CH target driven by a 12.4-kJ, 1-ns square OMEGA laser pulse. In this example, the target radius $R = 430$ μm, and the beam parameters $r_0 = 352$ μm and $n = 4.12$. The drive-laser pulse (long-dashed line) and calculated evolution of the absorption rates Q^s (solid lines) and $Q^{s,p}$ (short-dashed lines) for two values of the flux limiter $f_{\text{lim}} = 0.06$ and 0.1 are shown in Fig. 111.48(a). The reduced values of Q^s and $Q^{s,p}$ for smaller f_{lim} can be explained by an increased coronal temperature and, as a result, the less-efficient inverse bremsstrahlung absorption. Figure 111.48(b) shows the evolution of the relative difference $\left(Q^{s,p} - Q^s\right)/Q^s$ (solid lines),

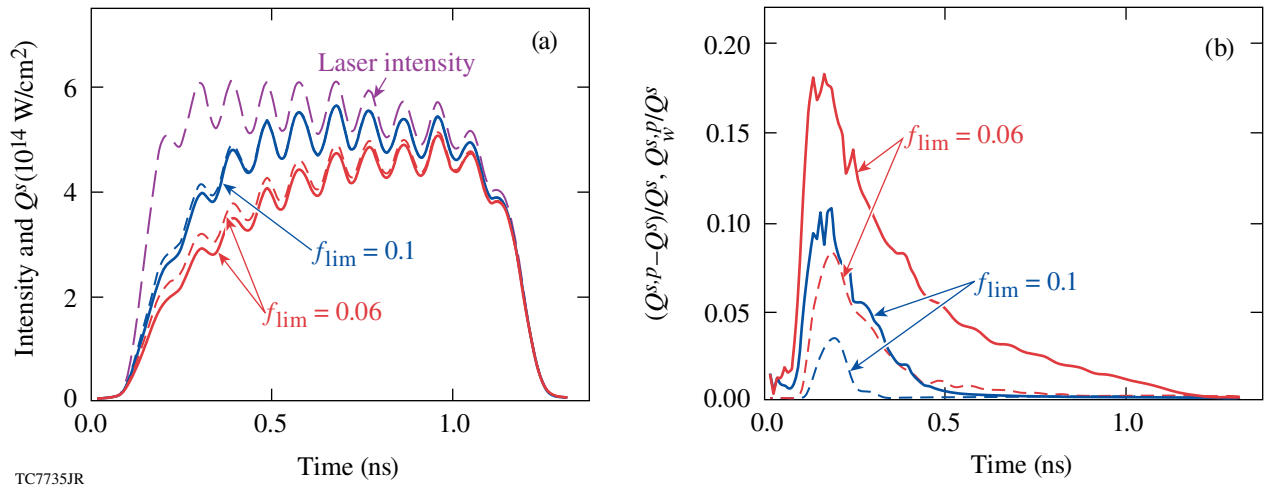

Figure 111.48
Simulated laser-absorption rates for two values of the flux limiter f_{lim} in the spherical implosion of a CH target driven by a 12.4-kJ, 1-ns OMEGA laser pulse. The approximate method to simulate the laser absorption in spherical implosions is discussed in the text. (a) Drive-laser pulse (long-dashed line) and absorption rates Q^s (solid lines) and $Q^{s,p}$ (short-dashed lines), for the *s*-polarized and mix-polarized (*s* and *p*) lights, respectively. The rate Q^s does not include the effect of resonant absorption, but $Q^{s,p}$ does. (b) The relative difference of absorption rates $\left(Q^{s,p}-Q^s\right)/Q^s$ (solid lines) and the relative absorption rates $Q_w^{s,p}/Q^s$ due to the resonant excitation of Langmuir waves (dashed lines).

which represents the relative effect of resonance absorption, and the ratio $Q_w^{s,p}/Q^s$ (dashed lines), where $Q_w^{s,p}$ represents a part of $Q^{s,p}$ due to the resonant excitation of Langmuir waves. Similar to the planar case (see Fig. 111.46), resonance absorption in spherical targets has a maximum effect at the beginning of the laser pulse, during the first 200 to 400 ps. Also, the resonantly excited Langmuir waves give a noticeable contribution to the total absorption only at the beginning of the laser pulse. The resonance absorption is reduced with an increase in f_{lim}. This reduction can be explained by an increase in the density scale length near the critical surface with an increase in f_{lim}. Based on the numerical results presented in Fig. 111.48(a), the effect of resonance absorption can be modeled with the standard laser ray-trace absorption method[26] by adjusting the flux limiter to a higher value (e.g., from the typical $f_{lim} = 0.06$ to 0.08) during the first ~200 ps of the pulse.

The dependence of resonance absorption on laser intensity in spherical implosions is demonstrated in Fig. 111.49 in the case of a 100-ps laser pulse. The pulse shape with a peak intensity of 5×10^{14} W/cm^2 (long-dashed line) and calculated absorption rates $Q^{s,p}$, Q^s, and $Q_w^{s,p}$ (thick solid, thin solid, and short-dashed lines, respectively) are shown in Fig. 111.49(a). The total absorption fractions calculated using these rates, integrated over the pulse duration, are shown in Fig. 111.49(b) [using the same notations as in Fig. 111.49(a)] as functions of the peak laser intensity. Note that the relative effect of resonant absorption has a weak dependence on the intensity. Specifically, this effect varies from about 13% to 20% for an intensity varied from 10^{14} to 10^{15} W/cm^2. The contribution of Langmuir waves to the total laser absorption varies from about 2% to 15% for the same range of intensity. Example absorption fractions in spherical implosion experiments on OMEGA employed ~100-ps drive pulses are shown in Fig. 111.49(b) by solid circles.

Planar Experiments

Two series of planar direct-drive experiments on OMEGA have been proposed to verify the model of resonance absorption presented in **Resonance Absorption in the Fluid Approximation** (p. 180): reflection-light experiments and shock-timing experiments. Both series are based on similar experimental designs employing a single OMEGA laser beam, either *s*- or *p*-polarized, which irradiates a CH foil. The experiments are designed for beams with $\theta = 23.2°$, which is one of the allowed values of θ, determined by the construction of the OMEGA target chamber, and close to the angle of the maximum effect of resonance absorption in OMEGA plasmas (see Fig. 111.47). The goal of these experiments is to demonstrate the relative effect of a resonance absorption mechanism by comparing reflection light and shock timing for the case of *s*- and *p*-polarized laser beams. In this section, the results of the reflection-light experiments are presented and compared with simulations, and the effect of resonance absorption in the proposed shock-timing experimental design is discussed.

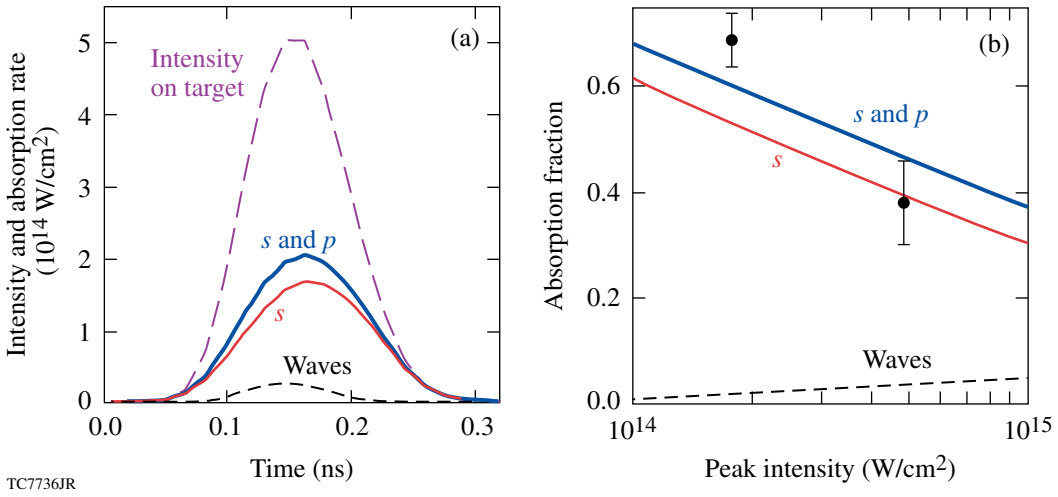

Figure 111.49
Simulated absorption rates and dependence of absorption fractions on the peak laser intensity in spherical implosions of a CH target driven by a 100-ps OMEGA laser pulse. The approximate method to simulate the laser absorption in spherical implosions is discussed in the text. (a) Drive-laser pulse (long-dashed curve); absorption rates calculated using an equal mixture of *s*- and *p*-polarized lights (thick solid line), and using only the *s*-polarized light (thin solid line); absorption rate due to the resonant excitation of Langmuir waves (short-dashed line). (b) Absorption fraction as a function of peak laser intensity for the same cases considered in (a) and in implosion experiments (solid circles), which include a mixture of *s*- and *p*-polarized lights. The effect of resonance absorption is represented by the difference in absorption rates and absorption fractions for the lights with mixed polarization and *s*-polarization.

The setup for the reflection-light experiments is shown schematically in Fig. 111.50. In these experiments, a 200-ps laser beam with an energy of 55 J (±5%) is propagated from port 23 [see Figs. 111.50(a) and 111.50(b)] toward a target and focused into a spot ~500 μm in diameter, resulting in an intensity $\approx 1.2 \times 10^{14}$ W/cm^2. The beam is smoothed in space and time by the spectral dispersion technique[39] and distributed phase plates.[40] The light reflected and scattered from the target is collected by three calorimeters located in ports 25, 17, and 30. The calorimeter in port 25 collects the specularly reflected light, whereas the other two calorimeters, in ports 17 and 30, collect the scattered light at about 23° from the direction to port 25. The calorimeter in port 17 is located on the target normal.

Table 111.V shows the beam energy along with the energy collected by the three calorimeters in two experiments with single *s*- and *p*-polarized OMEGA laser beams. In agreement with theory, which predicts smaller light reflection from the *p*-polarized beam, the energy reflected from the *s*-polarized beam exceeds the energy reflected from the *p*-polarized beam (both energies collected in port 25). Quantitatively, the experiments show a larger difference in these energies: the corresponding energy ratio is 2.5 versus 1.8 obtained in simulations. Figure 111.51 shows time-resolved reflected power in the experiments and simulations, where the simulation data (thin solid lines) are given in W/cm^2 and the experimental data

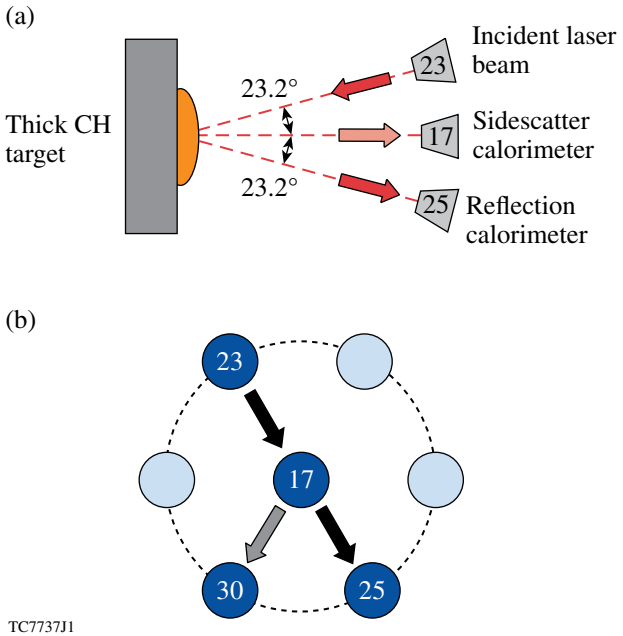

Figure 111.50
(a) Experimental setup for the reflection-light measurements, using single laser beams of *s*- or *p*-polarization. Port 17 is on the direction of target normal. (b) View of the OMEGA ports used in the experiment. Port 30 is not depicted in (a).

Table 111.V: Reflection- and scattered-light measurements. The experimental setup is illustrated in Fig. 111.50.

Beam polarization	Beam energy (J)	Collected Energy (J)		
		Port 25	Port 30	Port 17
s	52.5	1.59	0.15	0.14
p	57.1	0.63	0.17	0.22

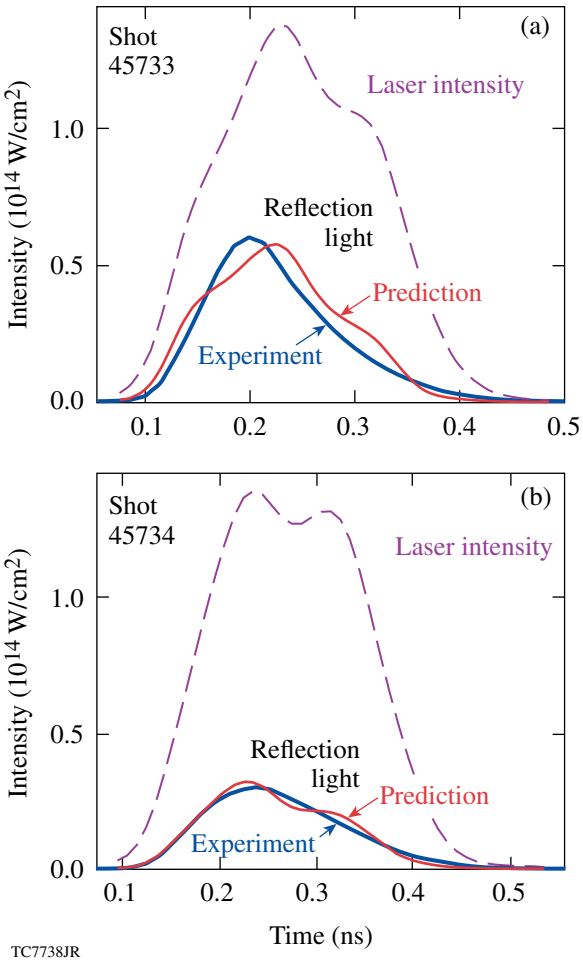

Figure 111.51
Time-resolved measured (thick solid lines) and simulated (thin solid lines) intensities of reflection light in the experiments illustrated in Fig. 111.50. The cases of (a) *s*-polarized and (b) *p*-polarized beams are shown. The incident laser intensities (in W/cm^2) are shown by the dashed lines. The simulated reflection data are presented in W/cm^2, whereas the experimental data are given in arbitrary normalizations.

(thick solid lines) use arbitrary normalizations. Note a good agreement of time profiles of the experimental and simulated energy fluxes in both cases of *s*- and *p*-polarized beams.

The reflection experiments revealed significant sidescatter of laser light in both cases of *s*- and *p*-polarized beams. Due to this scatter, the measured reflection energies are about an order of magnitude smaller than the values predicted in simulations. An estimate using the amount of energy scattered in ports 17 and 30 (see Table 111.V) and assuming a uniform scatter suggests that the total scattered energy exceeds the reflection energy by at least a factor of 20. A possible explanation for this scatter is the development of laser-induced perturbations of the reflection surface in plasma corona. These perturbations, or nonuniformities, can have spatial scales comparable to the laser wavelength and cause significant sidescatter of laser light if the amplitude of perturbations is large enough. The 1-D model of resonance absorption used in this article cannot consider perturbations in the transverse directions to the target normal and, therefore, cannot simulate such a scatter.

The early-time enhancement of laser absorption due to the resonance mechanism can affect the velocities of shocks originating at initial stages of implosions. A change in these velocities can be important for high-gain, direct-drive implosion designs that utilize adiabat-shaping techniques.[10,11] Shock-timing experiments, somewhat analogous to the shock-compressibility experiments,[41] can be suitable for the study of the effect of resonance absorption on shock properties.

The shock-timing experimental design uses a setup similar to that used in the reflection-light experiments (see Fig. 111.50). The measured quantity in this design is the velocity of shocks driven by the laser beams with different polarization. The effect of resonance absorption is estimated by comparing the shock-breakout times in finite-thickness targets in experiments with *s*- and *p*-polarized beams. On OMEGA, the shock-breakout time can be measured to an accuracy of about 50 ps by using two independent techniques: one that employs a velocity interferometer system for any reflector (VISAR),[42,43] and another that utilizes temporal records of the shock-front self-emission (600 to 1000 nm) acquired using an imaging streak camera.[44]

Figure 111.52 shows simulated time-dependent travel distances for two shocks driven by *s*- and *p*-polarized laser beams in thick CH targets. The simulations assume a 100-ps laser pulse, similar to one shown in Fig. 111.47(a), but with a peak intensity of 10^{14} W/cm^2. For a fixed travel distance, which corresponds to an assumed target thickness in experiments, the

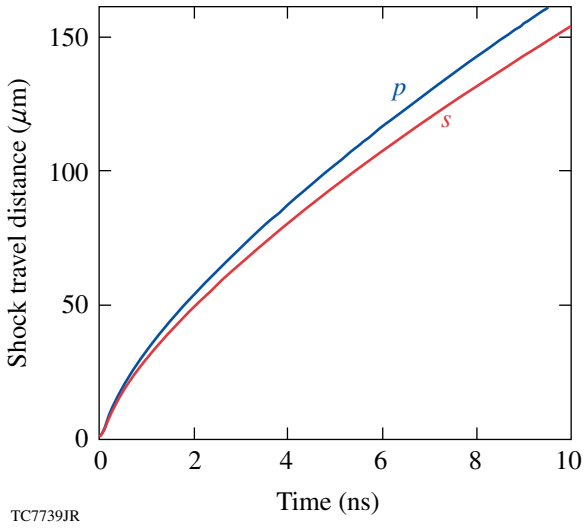

Figure 111.52
Simulated time dependence of the travel distance of shocks driven by single 100-ps OMEGA laser beams of different polarizations in thick CH foils. The beams have a peak intensity of 10^{14} W/cm^2 and $\theta = 23.2°$. Two cases of *s*- and *p*-polarized beams (marked by "*s*" and "*p*", respectively) are considered.

difference Δt between the propagation time of the two shocks corresponds to the difference of experimentally measured breakout time in the case of *s*- and *p*-polarized beams. The value Δt exceeds the experimental accuracy limit of 50 ps for targets thicker than 30 μm, and Δt is in the well-detectable range of several hundred picoseconds for target thicknesses $\gtrsim$100 μm. Specifically, one gets $\Delta t \approx$ 800 ps for a 125-μm-thick target.

Discussion and Conclusions

The effect of resonance absorption in a CH plasma has been investigated theoretically and experimentally for the physical conditions relevant to direct-drive ICF experiments with a 351-nm laser and intensities in the range of 10^{14} to 10^{15} W/cm^2. It has been shown that nonlinear effects, such as pondermotive force and wave breaking, are not important; therefore, the linear theory of resonance absorption has been used in the 1-D hydrodynamic code *LILAC* to construct numerical models. The resonant excitation of Langmuir waves at the critical surface is an important mechanism that contributes to resonance absorption and dominates inverse bremsstrahlung absorption in the case of laser intensities $\gtrsim 5 \times 10^{14}$ W/cm^2 and angles of incidence of laser beams in the optimum range, $10° \lesssim \theta \lesssim 30°$. The decay of Langmuir waves caused by Landau damping results in a release of wave energy in the form of hot electrons with temperature $\approx$5 keV, which is larger by a factor of 2 to 5 than the electron temperature in hot corona, where $T_e \approx$ 1 to 2 keV. This could lead to a deviation of the electron distribution function from Maxwellian in hot corona if the energy released in hot electrons is relatively large. In implosion experiments on OMEGA, however, this energy is predicted to be relatively low [less than 15% of the total absorbed energy (see the short-dashed lines in Fig. 111.49)], so that the coronal plasma there is expected to be nearly Maxwellian.

On OMEGA, resonance absorption has a maximum effect during a rapid increase in laser power, typically ~100 ps. Simulations show that the resonance absorption in a 1-ns square laser pulse can be important only during the first 200 to 300 ps. At this initial period, the density scale length in plasma near the critical surface is relatively short, ~1 to 2 μm, resulting in enhanced resonance absorption. At later times, when the laser power reaches its maximum, the density scale length increases to more than 5 μm, causing significant reduction in resonance absorption. In short laser pulses, or pickets, ~100 ps, the resonance absorption has a maximum relative effect, the value of which depends on the intensity and angle of incidence of the laser. In the case of spherical implosions, the predicted relative effect of resonance absorption varies from about 13% to 20% for intensities between 10^{14} and 10^{15} W/cm^2.

We suggest, based on our numerical results, that the resonance absorption in spherical implosions can be modeled with the standard laser ray-trace method,[26] using a time-variable flux limiter, the value of which is increased by ~30% during the first ~200 ps of the laser pulse.

Planar reflection-light experiments have been conducted on OMEGA to verify the theoretical predictions of resonance absorption. These experiments used CH foils irradiated by single *s*- and *p*-polarized laser beams with an angle of incidence $\theta = 23.2°$ and showed the reflection energy's clear dependence on polarization, in good quantitative agreement with simulation results. The experiments also revealed significant sidescatter of laser light, which reduces the amount of reflection energy by about an order of magnitude in comparison with simulations. This sidescatter, affecting both *s*- and *p*-polarized lights, can be explained by laser-induced perturbations in the reflection surface of plasma corona. The effect of these perturbations cannot be accounted for in the simplified 1-D approach used in this study. We expect that the surface perturbations could reduce the difference between reflected *s*- and *p*-polarized laser lights predicted in simulations because of the introduction of additional polarization components (mixed *s*- and *p*-polarized lights) in the incident laser beams.

Another OMEGA planar, direct-drive experiment that could demonstrate the effect of resonance absorption in laser-driven shocks has been designed and simulated. This design employs CH foils irradiated by single *s*- or *p*-polarized laser beams that initiate shocks with different velocities. The effect of resonance absorption is inferred by comparing the shock-breakout time at the target's rear surface in the case of *s*- and *p*-polarized beams. Assuming a 100-ps laser pulse with a peak intensity of 10^{14} W/cm^2, the simulations predict a time difference of shock breakout in the well-detectable range of several hundred picoseconds for a target thickness of about 100 μm.

ACKNOWLEDGMENT

This work was supported by the U.S. Department of Energy (DOE) Office of Inertial Confinement Fusion under Cooperative Agreement No. DE-FC52-92SF19460, the University of Rochester, the New York State Energy Research and Development Authority.

REFERENCES

1. J. D. Lindl, *Inertial Confinement Fusion: The Quest for Ignition and Energy Gain Using Indirect Drive* (Springer-Verlag, New York, 1998), pp. 39–52.
2. S. Atzeni and J. Meyer-ter-Vehn, *The Physics of Inertial Fusion: Beam Plasma Interaction, Hydrodynamics, Hot Dense Matter*, International Series of Monographs on Physics (Clarendon Press, Oxford, 2004), pp. 38–41 and 366.
3. R. L. McCrory, J. M. Soures, C. P. Verdon, F. J. Marshall, S. A. Letzring, S. Skupsky, T. J. Kessler, R. L. Kremens, J. P. Knauer, H. Kim, J. Delettrez, R. L. Keck, and D. K. Bradley, Nature **335**, 225 (1988).
4. S. E. Bodner, D. G. Colombant, J. H. Gardner, R. H. Lehmberg, S. P. Obenschain, L. Phillips, A. J. Schmitt, J. D. Sethian, R. L. McCrory, W. Seka, C. P. Verdon, J. P. Knauer, B. B. Afeyan, and H. T. Powell, Phys. Plasmas **5**, 1901 (1998).
5. P. W. McKenty, V. N. Goncharov, R. P. J. Town, S. Skupsky, R. Betti, and R. L. McCrory, Phys. Plasmas **8**, 2315 (2001).
6. P. W. McKenty, T. C. Sangster, M. Alexander, R. Betti, R. S. Craxton, J. A. Delettrez, L. Elasky, R. Epstein, A. Frank, V. Yu. Glebov, V. N. Goncharov, D. R. Harding, S. Jin, J. P. Knauer, R. L. Keck, S. J. Loucks, L. D. Lund, R. L. McCrory, F. J. Marshall, D. D. Meyerhofer, S. P. Regan, P. B. Radha, S. Roberts, W. Seka, S. Skupsky, V. A. Smalyuk, J. M. Soures, K. A. Thorp, M. Wozniak, J. A. Frenje, C. K. Li, R. D. Petrasso, F. H. Séguin, K. A. Fletcher, S. Padalino, C. Freeman, N. Izumi, J. A. Koch, R. A. Lerche, M. J. Moran, T. W. Phillips, G. J. Schmid, and C. Sorce, Phys. Plasmas **11**, 2790 (2004).
7. R. L. McCrory, S. P. Regan, S. J. Loucks, D. D. Meyerhofer, S. Skupsky, R. Betti, T. R. Boehly, R. S. Craxton, T. J. B. Collins, J. A. Delettrez, D. Edgell, R. Epstein, K. A. Fletcher, C. Freeman, J. A. Frenje, V. Yu. Glebov, V. N. Goncharov, D. R. Harding, I. V. Igumenshchev, R. L. Keck, J. D. Kilkenny, J. P. Knauer, C. K. Li, J. Marciante, J. A. Marozas, F. J. Marshall, A. V. Maximov, P. W. McKenty, J. Myatt, S. Padalino, R. D. Petrasso, P. B. Radha, T. C. Sangster, F. H. Séguin, W. Seka, V. A. Smalyuk, J. M. Soures, C. Stoeckl, B. Yaakobi, and J. D. Zuegel, Nucl. Fusion **45**, S283 (2005).
8. M. C. Herrmann, M. Tabak, and J. D. Lindl, Nucl. Fusion **41**, 99 (2001).
9. R. Betti, K. Anderson, V. N. Goncharov, R. L. McCrory, D. D. Meyerhofer, S. Skupsky, and R. P. J. Town, Phys. Plasmas **9**, 2277 (2002).
10. V. N. Goncharov, J. P. Knauer, P. W. McKenty, P. B. Radha, T. C. Sangster, S. Skupsky, R. Betti, R. L. McCrory, and D. D. Meyerhofer, Phys. Plasmas **10**, 1906 (2003).
11. K. Anderson and R. Betti, Phys. Plasmas **10**, 4448 (2003).
12. T. R. Boehly, D. L. Brown, R. S. Craxton, R. L. Keck, J. P. Knauer, J. H. Kelly, T. J. Kessler, S. A. Kumpan, S. J. Loucks, S. A. Letzring, F. J. Marshall, R. L. McCrory, S. F. B. Morse, W. Seka, J. M. Soures, and C. P. Verdon, Opt. Commun. **133**, 495 (1997).
13. N. G. Denisov, Sov. Phys.-JETP **4**, 544 (1957).
14. P. Hirsch and J. Shmoys, Radio Sci. J. Res. NBS/USNC–URSI **69D**, 521 (1965).
15. A. D. Piliya, Sov. Phys.-Tech. Phys. **11**, 609 (1966).
16. A. Ya. Omel'chenko and K. N. Stepanov, Ukr. Fiz. Zh. **12**, 1396 (1967).
17. T. Tang, Radio Sci. **5**, 111 (1970).
18. V. L. Ginzburg, *The Propagation of Electromagnetic Waves in Plasmas* (Pergamon Press, New York, 1970), pp. 319–438.
19. D. W. Forslund *et al*., Phys. Rev. A **11**, 679 (1975).
20. T. Speziale and P. J. Catto, Phys. Fluids **20**, 990 (1977).
21. G. J. Pert, Phys. Plasmas **20**, 175 (1978).
22. R. W. Means *et al*., Phys. Fluids **24**, 2197 (1981).
23. D. E. Hinkel-Lipsker, B. D. Fried, and G. J. Morales, Phys. Fluids B **4**, 559 (1992).
24. D. E. Hinkel-Lipsker, B. D. Fried, and G. J. Morales, Phys. Fluids B **4**, 1772 (1992); D. E. Hinkel-Lipsker, B. D. Fried, and G. J. Morales, Phys. Fluids B **5**, 1746 (1993).
25. H. Xu *et al*., Phys. Plasmas **13**, 123301 (2006).
26. J. Delettrez, R. Epstein, M. C. Richardson, P. A. Jaanimagi, and B. L. Henke, Phys. Rev. A **36**, 3926 (1987); J. Delettrez, Can. J. Phys. **64**, 932 (1986).
27. W. L. Kruer, *The Physics of Laser–Plasma Interactions*, Frontiers in Physics, Vol. 73, edited by D. Pines (Addison-Wesley, Redwood City, CA, 1988), Chap. 4, pp. 39–43.
28. F. F. Chen, *Introduction to Plasma Physics and Controlled Fusion*, 2nd ed., Vol. 1 (Plenum Press, New York, 1984), p. 87.

29. E. M. Lifshitz and L. P. Pitaevskifi, *Physical Kinetics*, 1st ed., Course of Theoretical Physics, Vol. 10 (Pergamon Press, Oxford, 1981), pp. 124–127.

30. W. H. Press *et al*., *Numerical Recipes in FORTRAN: The Art of Scientific Computing*, 2nd ed. (Cambridge University Press, Cambridge, England, 1992), pp. 34–38.

31. L. Spitzer, Jr. and R. Härm, Phys. Rev. **89**, 977 (1953).

32. A. B. Langdon, Phys. Rev. Lett. **44**, 575 (1980).

33. A. Sunahara, J. A. Delettrez, C. Stoeckl, R. W. Short, and S. Skupsky, Phys. Rev. Lett. **91**, 095003 (2003).

34. G. P. Schurtz, Ph. D. Nicolaï, and M. Busquet, Phys. Plasmas **7**, 4238 (2000).

35. V. N. Goncharov, O. V. Gotchev, E. Vianello, T. R. Boehly, J. P. Knauer, P. W. McKenty, P. B. Radha, S. P. Regan, T. C. Sangster, S. Skupsky, V. A. Smalyuk, R. Betti, R. L. McCrory, D. D. Meyerhofer, and C. Cherfils-Clérouin, Phys. Plasmas **13**, 012702 (2006).

36. S. Skupsky, R. W. Short, T. Kessler, R. S. Craxton, S. Letzring, and J. M. Soures, J. Appl. Phys. **66**, 3456 (1989).

37. T. P. Coffey, Phys. Fluids **14**, 1402 (1971).

38. S. P. Regan, J. A. Marozas, R. S. Craxton, J. H. Kelly, W. R. Donaldson, P. A. Jaanimagi, D. Jacobs-Perkins, R. L. Keck, T. J. Kessler, D. D. Meyerhofer, T. C. Sangster, W. Seka, V. A. Smalyuk, S. Skupsky, and J. D. Zuegel, J. Opt. Soc. Am. B **22**, 998 (2005).

39. S. Skupsky and R. S. Craxton, Phys. Plasmas **6**, 2157 (1999).

40. Y. Lin, T. J. Kessler, and G. N. Lawrence, Opt. Lett. **21**, 1703 (1996).

41. T. R. Boehly, E. Vianello, J. E. Miller, R. S. Craxton, T. J. B. Collins, V. N. Goncharov, I. V. Igumenshchev, D. D. Meyerhofer, D. G. Hicks, P. M. Celliers, and G. W. Collins, Phys. Plasmas **13**, 056303 (2006).

42. L. M. Barker and R. E. Hollenbach, J. Appl. Phys. **43**, 4669 (1972).

43. P. M. Celliers, D. K. Bradley, G. W. Collins, D. G. Hicks, T. R. Boehly, and W. J. Armstrong, Rev. Sci. Instrum. **75**, 4916 (2004).

44. J. E. Miller, T. R. Boehly, E. Vianello, W. J. Armstrong, C. Sorce, W. Theobald, D. D. Meyerhofer, D. G. Hicks, J. H. Eggert, and P. M. Celliers, Bull. Am. Phys. Soc. **50**, 60 (2005); J. A. Oertel *et al*., Rev. Sci. Instrum. **70**, 803 (1999).